The Astrophysical Journal Letters, 990:L22 (10pp), 2025 September 1 https://doi.org/10.3847/2041-8213/adfa21

Temperatures of Jupiter's Upper Atmosphere: The Role of the Planetary Magnetic Field

Ingo C. F. Müller-Wodarg[1], Peio Iñurrigarro[1], Luke Moore[2], Tommi T. Koskinen[3], and Alexander S. Medvedev[4]
[1] Department of Physics, Imperial College London, UK; i.mueller-wodarg@imperial.ac.uk
[2] Center for Space Physics, Boston University, USA
[3] Lunar & Planetary Laboratory, University of Arizona, USA
[4] Max Planck Institute for Solar Systems Research, Germany
Received 2025 June 12; revised 2025 August 7; accepted 2025 August 10; published 2025 August 29

Abstract

The primary source of heating in the upper atmospheres (thermospheres) of giant planets has been the subject of long debate. The conundrum (or "energy crisis") consists in observed thermosphere temperatures at low and midlatitudes exceeding values expected from solar heating by several hundred kelvins, suggesting the presence of another energy source. Several theories have been proposed to explain the high temperatures, from heating by upward-propagating gravity or acoustic waves to heating of auroral regions by magnetosphere–atmosphere coupling. While auroral heating provides sufficient energy, the problem becomes one of global energy redistribution. On a rapidly rotating planet, Coriolis forces act to "trap" auroral energy in the polar regions, heating up the poles but leaving the equator cold. On Saturn, the redistribution of energy from poles to equator was recently achieved by invoking Rayleigh drag, possibly related to atmospheric gravity or acoustic waves. Using a new general circulation model of Jupiter, we reproduce well the observed low and midlatitude thermosphere temperatures without the need to invoke Rayleigh drag. Instead, the planet's magnetic field is strong enough to cause significant ion drag and slowing down zonal winds in the nonauroral thermosphere and allow global energy redistribution. This distinguishes Jupiter from Saturn and most likely the other gas giant planets in our solar system may have implications on extrasolar planets with strong magnetic fields as well.

Unified Astronomy Thesaurus concepts: Planetary atmospheres (1244); Planetary science (1255); Jupiter (873); Planetary ionospheres (2185); Theoretical models (2107); Planetary magnetospheres (997)

1. Introduction

The upper atmosphere of Jupiter is a transition region between the atmosphere and the space environment, its vast magnetosphere. Manifestations of the magnetosphere–atmosphere interaction are the auroral emissions that were first observed in the UV (A. L. Broadfoot et al. 1979) and later in the IR (P. Drossart et al. 1989), allowing us to study by remote sensing the interaction between Jupiter's ionosphere and middle magnetosphere.

The nature of the interaction between Jupiter's atmosphere and magnetosphere was first described by T. W. Hill (1980), whereby material emitted via Io's volcanic eruptions forms the main source of initially neutral particles (including sulfur and sulfur dioxide) in Jupiter's magnetosphere that over time become ionized by solar radiation, energetic electron impact, and cosmic rays and form the main plasma sheet in the equatorial plane. The material from Io initially orbits the planet at a Keplerian period (42.459 hr), while the magnetosphere rotates at the planet's rotation period (9.925 hr). Once ionized, the material is picked up by the magnetic field and brought to corotation with the magnetosphere via a system of field-aligned currents that close through the Jovian ionosphere equatorward across the main auroral oval (S. W. H. Cowley & E. J. Bunce 2001). The field-aligned current system extracts angular momentum from the atmosphere and transfers it to the magnetosphere plasma. The continuous deposition of new material from Io into the magnetosphere maintains the field-aligned current system and transfer of angular momentum. Precipitation of energetic electrons along the magnetic field lines into the upper atmosphere near the magnetic poles causes excitation of atmospheric gas particles and generates Jupiter's auroral emissions. While the above description is consistent with the broad consensus of the past few decades, recent observations have indicated that the detailed picture is—of course—more complicated (B. Bonfond et al. 2020).

Particle precipitation furthermore leads to particle impact ionization and local heating of atmospheric gases, considerably contributing to the ionospheric plasma densities in auroral regions. Magnetospheric electric fields are mapped along magnetic field lines into the auroral region. The mainly meridionally directed electric field drives westward (against the sense of planet rotation) plasma jets at pressures where the ionospheric Pedersen conductivities maximize (T. W. Hill 1980; R. Prangé 1992; S. W. H. Cowley & E. J. Bunce 2001). Within the Pedersen layer of the ionosphere, collisions between ions and neutral gas particles exert a frictional torque on the magnetospheric flux tubes, bringing them toward corotation with the atmosphere (S. W. H. Cowley & E. J. Bunce 2001). From the atmosphere's frame of reference, this momentum transfer between atmosphere and magnetosphere is seen as a westward neutral wind acceleration, against the planet's rotation. So, magnetosphere–atmosphere coupling causes angular momentum transfer from atmosphere to magnetosphere that is manifested within the atmosphere as a substantial westward jet in Jupiter's auroral regions that can reach several km s^{-1} (T. Stallard et al. 2001).

Alongside this momentum coupling, the field-perpendicular currents within the ionosphere also lead to frictional heating ("Joule heating"), a major energy source within the upper atmosphere contributing around 100 TW of energy (D. F. Strobel 2002). This value exceeds the solar energy influx (around 1 TW) by several orders of magnitude, highlighting the fact that the magnetosphere interaction provides a major energy source in Jupiter's upper atmosphere. Therefore, the question arises whether magnetosphere–ionosphere coupling can explain the large thermosphere temperatures at low to midlatitudes detected on Jupiter (around 940 K) where solar heating alone would generate around 203 K (R. V. Yelle & S. Miller 2004). Can the plentiful auroral energy be redistributed effectively on the fast-spinning planet, something that recent simulation studies suggested as being challenging, especially on Saturn (C. G. A. Smith et al. 2007; I. C. F. Müller-Wodarg et al. 2019)?

On fast-spinning planets like Saturn, the Coriolis forces efficiently divert any pole-to-equator winds into the zonal direction (east–west), thereby preventing the transport of energy from pole to equator. A slow equator-to-pole flow in the deep thermosphere (below 1000 km on Saturn) further cools down the equator (C. G. A. Smith et al. 2007), making the equatorial temperatures far cooler than observed. The inability to theoretically reproduce equatorial temperatures is often referred to as the giant gas planet "energy crisis" (R. V. Yelle & S. Miller 2004). Part of our motivation for the following study is to understand the global thermal structure on Jupiter as compared with Saturn.

In the following, we present a new model to simulate the complex magnetosphere–atmosphere interaction in 3D, the Jupiter Thermosphere Ionosphere Model (JTIM). This general circulation model (GCM) joins a family of existing Jupiter thermosphere–ionosphere GCMs (N. Achilleos et al. 1998; S. W. Bougher et al. 2005; C. Tao et al. 2009; J. N. Yates et al. 2020) and is based on the Saturn Thermosphere Ionosphere Model (STIM; L. E. Moore et al. 2004; I. C. F. Müller-Wodarg et al. 2006, 2012, 2019; P. Iñurrigarro et al. 2024). Section 2 outlines the basic framework of JTIM and the auroral input parameters (convection electric field and electron precipitation) chosen for our simulations. Section 3 discusses our simulation results and comparisons with experiments in which we alter the planet's magnetic field geometry and strength. The implications of our findings are discussed in Section 4.

2. The Model

The JTIM is based on a similar model for Saturn, the STIM (L. E. Moore et al. 2004; I. C. F. Müller-Wodarg et al. 2006, 2012, 2019; P. Iñurrigarro et al. 2024). JTIM numerically integrates the time-dependent coupled Navier–Stokes equations of momentum, energy, and continuity for neutral gases and ions on a global spherical pressure grid with flexible horizontal and vertical resolution. The lower boundary of JTIM is located at 9.5 Pa (95 μbar), and the upper boundary is at $4.4 \cdot 10^{-8}$ Pa. We map the lower boundary pressure to a globally uniform altitude of 200 km above the 1 bar level where we assume as boundary conditions a globally uniform temperature of 165 K and zero horizontal wind speeds. While the assumption of zero horizontal winds near 9.5 Pa is not expected to be realistic, according to preliminary tests, this will not affect this study. Future studies will explore different boundary conditions and their effects more systematically. Like STIM, JTIM treats the absorption of solar radiation in the UV self-consistently via line-of-sight integration (using the Beer–Lambert law), assuming a heating efficiency of 50% for all constituents and wavelengths (J. H. Waite et al. 1983). Given the low importance of solar radiation as a direct heating mechanism, the choice of this value has little effect on our results, as was also explored with STIM for Saturn (I. C. F. Müller-Wodarg et al. 2006). Solar radiation absorption also generates ionization, which in turn triggers ion–ion and ion–neutral chemical reactions as outlined by L. E. Moore et al. (2004), whose reaction rates and ionization cross sections we assume in JTIM.

At auroral latitudes (10°–16° magnetic colatitude), we use parameterized height- (pressure-) dependent particle impact ionization rates for H^+, H_2^+, and He^+ from D. Grodent et al. (2001). We assume the auroral electric field of S. W. H. Cowley et al. (2005), which is aligned with the magnetic coordinate system and can be scaled in its strength. The imposed external electric field ($\boldsymbol{E}$ in Equation (A7)) reaches to around 17° magnetic colatitude in both hemispheres and is set to zero equatorward of that. We use the JRM33 magnetic field model of J. E. P. Connerney et al. (2022) and the resulting magnetic coordinate system derived by Y. Wang et al. (2023). Externally driven by user-defined solar radiation and magnetospheric forcing conditions, JTIM self-consistently calculates global time-dependent profiles of temperatures and winds and neutral gas, ion, and electron densities. Horizontal and vertical transport of neutral gases H, H_2, and He by winds and molecular and eddy diffusion are also treated self-consistently. The JTIM model is described in detail in the Appendix.

3. Simulations

To simulate a "standard" atmosphere with JTIM, we assume solar minimum conditions, high-latitude electric fields based on S. W. H. Cowley et al. (2005) with a peak strength of $1.2\ \mathrm{V\,m^{-1}}$, and the auroral impact ionization rates of D. Grodent et al. (2001). The magnetospheric electric fields drive currents in the auroral ionosphere at pressures where Pedersen conductivities are largest (around 0.02 μbar), causing Joule heating and westward (anticorotational) acceleration of neutral winds, as described in the Appendix. The solar cycle conditions have a minimal effect on direct solar heating of the thermosphere but will affect ionospheric conductivities, particularly at equatorial latitudes. We find that, globally averaged, temperatures increase by 70 K from solar minimum to solar maximum due to larger electron densities and Joule heating.

Figure 1 shows comparisons between temperatures calculated by JTIM (black lines; zonally averaged) and observations by the Galileo Atmospheric Structure Instrument (ASI) in 1995 (A. Seiff et al. 1997; left panel) as well as H_3^+ temperatures observed with the Keck II telescope in 2016 and 2017 (J. O'Donoghue et al. 2021; right panel). JTIM does not explicitly calculate the temperature of H_3^+, but H_3^+ temperatures are regarded as a good proxy for neutral temperatures (R. V. Yelle & S. Miller 2004). In order to be roughly consistent with the processing of observations, JTIM neutral temperatures in the right panel (solid line) are weighted by the H_3^+ densities in the model, thus representing temperatures from primarily the 10^{-2} μbar region, where H_3^+ densities are largest.

In both profiles, the match between simulations and observations is very good, illustrating that JTIM reproduces well the lower thermosphere region where vertical temperature

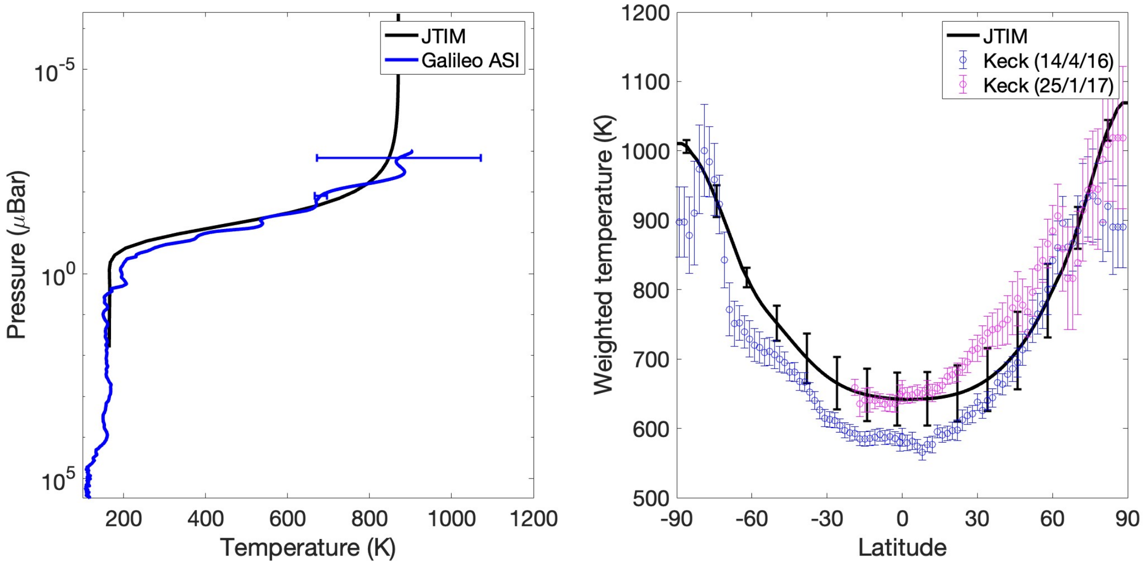

Figure 1. Comparison between temperatures calculated by JTIM (black lines; zonally averaged) and observations. Left panel: vertical profile of temperatures from the Galileo ASI taken on 1995 December 7 near 6.°5N and 4.°9W (A. Seiff et al. 1997). The ±200 K uncertainty in the temperature near 10^{-3} μbar (around 1000 km) as given by A. Seiff et al. (1997) is also shown, as is the ±15 K uncertainty near 10^{-2} μbar (around 700 km). Right panel: latitudinal profiles of temperatures measured with the Near-InfraRed Spectrometer mounted on the 10 m Keck II telescope in 2016 April and 2017 January (J. O'Donoghue et al. 2021). In the right panel, diurnal variability of temperatures in JTIM is represented by error bars on the black line. Temperatures in the right panel are integrated vertically, weighted at each level by the local H_3^+ column densities and divided by the total column density of H_3^+, thus representing temperatures from primarily the 10^{-2} μbar region, where H_3^+ densities are largest.

gradients are largest and reproduces well the observed pole-to-equator temperature profiles. This is in stark contrast to what was found by GCMs for Saturn, where the models produced correct auroral temperatures but underestimated the equatorial temperatures by several hundred kelvins (C. G. A. Smith et al. 2007; I. C. F. Müller-Wodarg et al. 2012, 2019). Those authors attributed the cold equatorial regions to the auroral energy being "trapped" in the polar regions by Coriolis forces. Our simulations in Figure 1, however, suggest no such difficulty in reproducing temperatures on Jupiter, unlike what had previously been found on Saturn (I. C. F. Müller-Wodarg et al. 2012, 2019).

To further illustrate this difference between Jupiter and Saturn, Figure 2 shows latitudinal profiles of normalized exospheric temperature simulated by JTIM for Jupiter (solid line) and STIM for Saturn (dashed line). For clarity, we show the southern hemisphere only. At Jupiter, the model produces a shallow temperature gradient from pole to equator with equatorial values being around 85% of polar values. For Saturn, equatorial temperatures are around 40% of the polar values. On both planets, the main energy source is magnetosphere–atmosphere coupling, with direct solar heating playing a minor role only. The question therefore arises as to why pole-to-equator energy transport appears to work on Jupiter while not being efficient on Saturn The broader significance of this is whether the "energy crisis" is unique to Saturn.

In their efforts to reproduce the observed large equatorial temperatures on Saturn, I. C. F. Müller-Wodarg et al. (2019) highlighted the role played by atmospheric dynamics in shaping the global temperature structure. For the case of Saturn, they found that invoking an extra Rayleigh momentum drag possibly related to atmospheric waves in the zonal direction at high midlatitudes would slow down the strong zonal winds sufficiently to overcome the "Coriolis barrier" and allow pole-to-equator transport of energy. No such additional drag was needed for Jupiter in our simulations. The Saturn

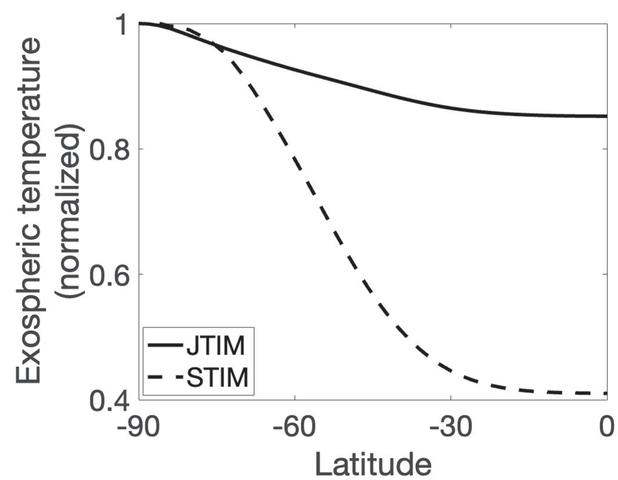

Figure 2. Latitudinal profiles of normalized temperatures in the southern hemisphere at the top of the thermosphere ("exospheric temperatures") as simulated by the JTIM model for Jupiter (solid line) and the STIM (I. C. F. Müller-Wodarg et al. 2012, 2019) for Saturn. Both STIM and JTIM use the same dynamical cores and can be directly compared.

simulation shown in Figure 2 (dashed line) did not include the artificial Rayleigh drag (thereby giving the cold equator), allowing direct comparison with the Jupiter simulation.

On planets with an internal magnetic field such as Jupiter and Saturn, the ions are tied to the magnetic field lines in regions where the ion gyrofrequency exceeds the ion–neutral collision frequency. On Jupiter, typical ion gyrofrequencies are around $\sim 10^4$ s^{-1} and in the JTIM atmosphere exceed ion–neutral collision frequencies at pressures below around $p \leqslant 0.1$ μbar. In those regions, the presence of ions can exert an additional drag on the neutral gases via collisions. When external electric fields are present (in the auroral regions), the collisions between ions and neutrals, in turn, lead to acceleration of the neutral gases by the ions.

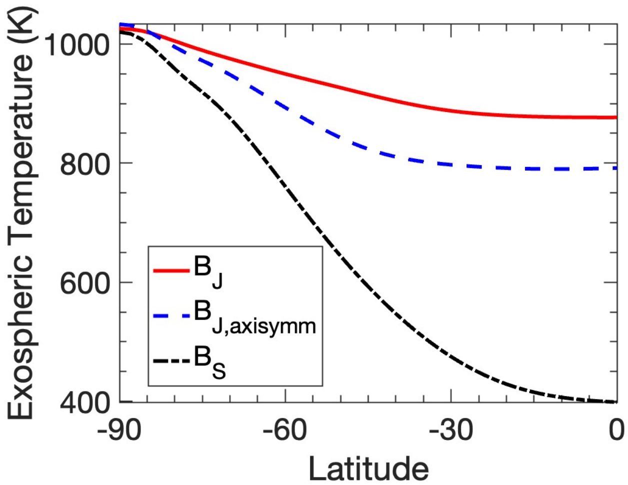

Figure 3. Zonally averaged southern hemisphere exospheric temperatures on Jupiter from our standard simulation (red solid), an experiment where we make the Jovian ***B***-field axisymmetric (blue dashed), and an experiment where we implement an axisymmetric Saturnian ***B***-field (black dashed–dotted).

As can be seen from the expressions for the meridional and zonal ion drag terms in the momentum equations of JTIM and STIM, $a_{\mathrm{idrag}\ \theta} = B_r j_\phi / \rho$ and $a_{\mathrm{idrag}\ \phi} = -B_r j_\theta / \rho$, respectively (where B_r is the radial B-field component, ρ is the atmospheric mass density, and j_θ and j_ϕ are the meridional and zonal components of current density given by Equations (A9) and (A10)), it is sensitive to the planetary magnetic field, $\boldsymbol{B}$. Therefore, the question arises whether the differences between Jupiter and Saturn (Figure 2) can be related to their differences in planetary magnetic field. To investigate this further, we present two further numerical experiments with JTIM.

In the first experiment, we change the Jovian ***B***-field in JTIM to axisymmetric (removing the $\sim$10° dipole tilt), thereby making the magnetospheric Joule heating and momentum forcing zonally symmetric. The intent is to investigate whether the offset of the Jovian magnetic and rotation axes could cause the differences in Figure 2, given that one prominent feature of Saturn's ***B***-field is its near axisymmetry. In the second experiment, we set the ***B***-field in JTIM to the Saturn ***B***-field from L. J. Davis & E. J. Smith (1990), removing higher-order terms to make it perfectly axisymmetric. Here, the magnetic and geographic axes (and coordinates) are made to coincide, resulting in axisymmetric auroral forcing. With the reduced (Saturnian) ***B***-field strength in the second experiment, we also have to adjust the electric field strength in that simulation, reducing it by a factor of 15 (giving a maximum field strength of 0.08 V m^{-1}) to obtain the same auroral temperatures. With a reduced ambient ***B***-field, the conductivities are enhanced, and thereby the currents and the Joule heating rates, so without the electric field adjustment in the second experiment, the auroral temperatures would have been much higher than in the simulations with the Jovian ***B***-field.

The results of our experiments are shown in Figure 3 and compared with our "standard" Jovian simulation of Figures 1 and 2 (shown as a red line). Again, we show the southern hemisphere only. Making the ***B***-field axisymmetric in our simulations (blue line in Figure 3) reduces the equatorial temperature by around 80 K compared with the "standard" case (red line), thereby contributing to some extent to the pole-to-equator temperature difference. Changing the ***B***-field to the (weaker) Saturnian field in our second experiment (black line), the equatorial temperature is reduced by around 480 K with respect to the "standard" case (red line) while having the same polar temperature. This result indicates that the strength of the planetary ***B***-field and, to second order, its geometry play key roles in the global redistribution of energy on giant planets.

To understand the underlying physical processes better, Figure 4 compares three key parameters on Jupiter and Saturn from calculations by JTIM from our "standard" simulation (upper row, panels (A)–(C)) and from STIM for an equinox simulation at Saturn without the Rayleigh drag of I. C. F. Müller-Wodarg et al. (2019; lower row, panels (D)–(F)). All quantities in the figure are zonal averages. We will first discuss the Jupiter results (upper row).

Zonal wind speeds, u_ϕ (A), are predominantly westward and reaching 850 m s^{-1}, driven by the magnetospheric electric field and representing the transfer of angular momentum into the magnetosphere. The meridional winds as a fraction of zonal wind speed ($u_\theta/|u_\phi|$) (B) reach values of $\pm$1.5, indicating that in some regions the flow is more meridional than zonal. Noteworthy is the "tongue," a region near 10^{-3}–10^{-4} μbar equatorward of around $-60°$ latitude where the meridional winds are enhanced, reaching 1.5 times the zonal wind and pointing northward (toward the equator, away from the pole). This region of enhanced meridional winds coincides with a region of reduced zonal winds (A). Panel (C) shows that the region coincides with enhanced eastward zonal ion drag ($a_{ni,\phi}$), pointed against the westward zonal wind direction. In the region of positive (eastward) ion drag in (C), the zonal winds are slowed down, leading to a change in the momentum balance in favor of enhanced pressure-gradient-driven equatorward meridional winds of around 160 m s^{-1} that generate energy transport from the pole toward the equator. Thereby, the "tongue" that we see on Jupiter but not on Saturn is a direct consequence of Jupiter's stronger magnetic field. Near the polar region in (C), the ion drag is westward due to the magnetospheric electric fields, accelerating the zonal winds toward the west.

For the case of Saturn (lower row, panels (D)–(F)), the zonal wind speeds are, like Jupiter's, predominantly westward, reaching 1500 m s^{-1}. The $u_\theta/|u_\phi|$ values (E) reach $\pm$0.3 at their peak, about a factor of 5 smaller than on Jupiter. Ion drag (F) is, like on Jupiter, westward (negative; blue) near the pole and eastward (positive; yellow) elsewhere, equatorward of around $-70°$ latitude where it slows down ("drags") the zonal winds. In the "drag" region, the term reaches around 7×10^{-2} m s^{-2} on Jupiter and 5×10^{-3} m s^{-2} on Saturn, so the zonal drag slowing down the neutral gases via collisions with ions is a factor of 10–15 larger on Jupiter, slowing down the zonal winds more effectively on Jupiter than on Saturn and causing larger equatorward winds on Jupiter ($\sim$160 m s^{-1}) than on Saturn ($\sim$15 m s^{-1}) in the regions of peak ion drag (positive peaks in (C) and (F)).

It is of interest to compare the locations of the "ion drag regions" (equatorward of 70°S) where the ion drag slows down thermosphere winds on both planets. As can be seen from panels (C) and (F) in Figure 4, they are strongest at around 2×10^{-3} μbar on Jupiter and 1×10^{-4} μbar on Saturn, so deeper in the atmosphere on Jupiter. This is due to the differences in the ***B***-field strength and means that the drag is at a level on Jupiter where the neutral densities are larger too. In our calculations, we find the neutral gas densities in the Jupiter "drag region" to be around 2×10^{15} m^{-3} compared with

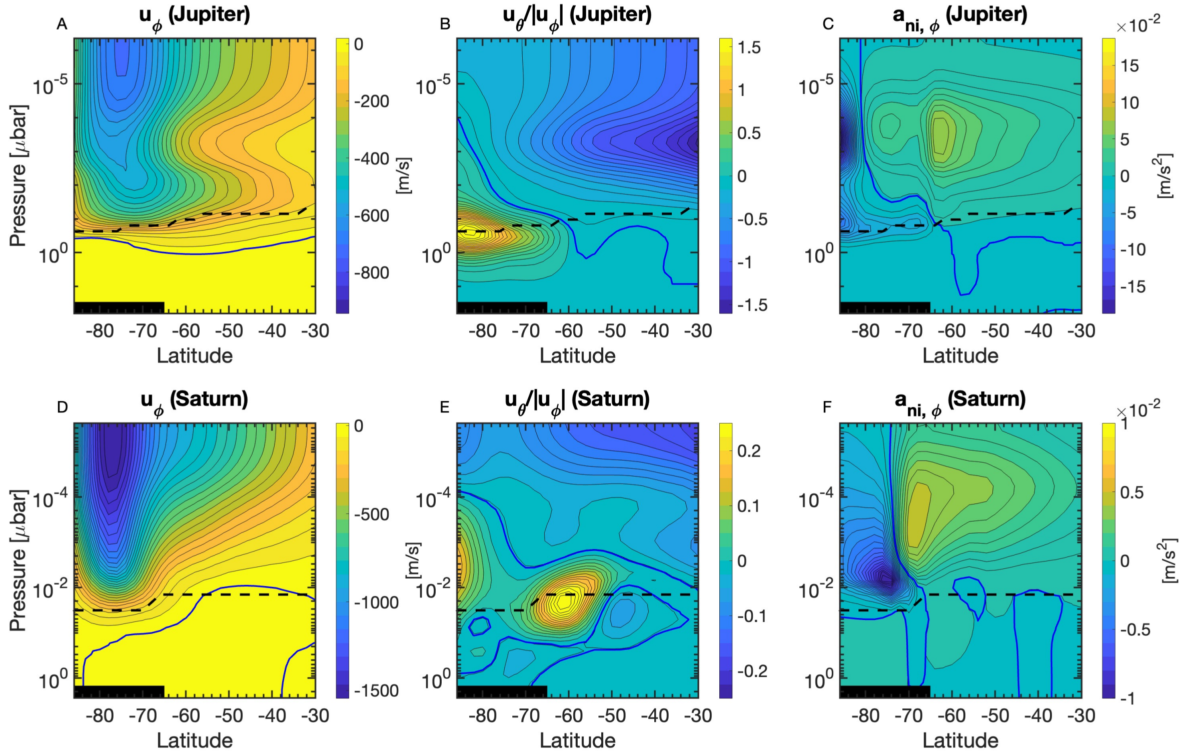

Figure 4. Zonally averaged parameters from global simulations by the JTIM model for Jupiter (upper row) and the STIM model for Saturn (lower row). The first column (panels (A) and (D)) gives zonal wind speeds u_ϕ (positive eastward), the second column ((B) and (E)) gives the ratios of meridional wind speed to the absolute of zonal wind speed $u_\theta/|u_\phi|$ (positive southward), and the third column ((C) and (F)) gives the zonal ion drag term ($a_{ni,\phi}$; Equation (A6)). The dashed line in each panel indicates the region where the Pedersen conductivity peaks. Contours in panels (A) and (D) are in m s^{-1}, (B) and (E) are unitless, and (C) and (F) are in m s^{-2}. Blue solid lines indicate the zero values. The zonal wind speeds in panels (A) and (D) reach positive (eastward) values of 20 m s^{-1} and 15 m s^{-1}, respectively. Thick black lines on the x-axes indicate the regions of auroral forcing on both planets.

1.3×10^{15} m^{-3} on Saturn, giving ion–neutral collision frequencies of around 111 s^{-1} and 9 s^{-1}, respectively. The ion gyrofrequencies on both planets at those locations are around 9×10^4 s^{-1} on Jupiter and 4×10^3 s^{-1} on Saturn, so the drag peaks on both planets where the ratio of collision frequency to gyrofrequency is around 10^{-3}.

4. Discussion

The described differences between Jupiter and Saturn can be attributed to the differences in their $\boldsymbol{B}$-field strengths in their mid- and high-latitude thermospheres ($\sim$1–10 $\times 10^{-4}$ T and $\sim$0.1–0.4 $\times 10^{-4}$ T, respectively). Thereby, the strength of the planet's $\boldsymbol{B}$-field is seen to directly influence the neutral gas dynamics and, in turn, the global energy distribution in the upper atmosphere. While coupling of the upper atmosphere to the magnetosphere at high latitudes is well known to exert a key influence on the upper atmosphere's energy and momentum budget, the role of the $\boldsymbol{B}$-field outside of the auroral region has hitherto been less appreciated. Outside of the auroral region, we assume a zero electric field, so $\boldsymbol{E}$ in Equation (A7) is zero and Equation (A6), the ion drag term in JTIM, reduces to $\boldsymbol{a}_{ni} = 1/\rho \cdot \underline{\sigma} \cdot (\boldsymbol{u} \times \boldsymbol{B}) \times \boldsymbol{B}$, where ρ is the mass density, $\underline{\sigma}$ denotes the conductivity tensor, and $\boldsymbol{u}$ is the neutral wind velocity vector. We currently ignore wind-driven dynamo electric fields in JTIM but consider including these in future versions of the code, following the implementation into STIM described by J. W. Vriesema et al. (2020).

In particular, our calculations suggest that the $\boldsymbol{B}$-field has a direct role in resolving the giant planet "energy crisis" in that the $\boldsymbol{B}$-field on Jupiter allows for meridional energy transport from poles to equator, thereby accounting for the observed unexpectedly high temperatures at low and midlatitudes. On Saturn, the $\boldsymbol{B}$-field is too weak to provide the additional needed zonal ion drag to slow down the zonal wind speeds and allow pole-to-equator energy transport. There, such transport could be enabled by Rayleigh drag in the atmosphere (I. C. F. Müller-Wodarg et al. 2019), possibly related to atmospheric waves (Z. L. Brown et al. 2022). Interestingly, the geometry of the $\boldsymbol{B}$-field (offset between magnetic and rotation axes) has a smaller-than-expected influence on Jupiter and Saturn upper atmosphere energy distribution.

More broadly, what do these findings allow us to conclude about the other giant planets in our solar system, Uranus and Neptune? Their surface $\boldsymbol{B}$-fields at the dipole equators are 22,800 nT and 14,200 nT, respectively, comparable to Saturn's (21,400 nT) and considerably smaller than Jupiter's (430,000 nT) (F. Bagenal 2013). This suggests that ion drag may be less efficient at slowing down neutral winds in their upper atmospheres outside the auroral regions. However, the extreme dipole tilts at Uranus and Neptune ($-59°$ and $-47°$, respectively) are likely to play a more significant role than we found for Jupiter ($-9\overset{\circ}{.}4$ tilt) in affecting global energy redistribution. On Uranus and Neptune, these extreme tilts may well lead to well-mixed upper atmospheres and efficient distribution of auroral energy, possibly resolving the "energy crisis" on those planets—if correct, highlighting the unique situation of Saturn. Studying the effect of magnetosphere–ionosphere coupling on the energy and dynamics of Uranus's and Neptune's upper atmospheres requires future modeling efforts. While JTIM still has some inherent simplifications, these are not likely to have any major effect on the conclusions of our study. Future studies will address the effects of coupling to the deeper atmosphere via atmospheric waves and a more realistic description of the magnetospheric electric fields and precipitation patterns as well as the footprints of Galilean moons. While we assumed a fixed auroral pattern in the magnetic frame that does not change with time (though allowing for local time changes at any fixed location on the rotating planet), we will in the future explore the effects of variable auroral patterns. Finally, self-consistent coupling to a magnetospheric MHD model, while posing computational challenges due to the different physical regimes, is a medium-term goal.

5. Conclusion

In comparing the calculated pole-to-equator temperature distributions on Jupiter and Saturn, we have found a hitherto-unexplored role that the planetary ***B***-field plays. While previous work suggested that redistribution of auroral energy was taking place on Jupiter (T. Majeed et al. 2009), we now understand the difference between it and Saturn without the need to invoke Rayleigh-type atmosphere drag (I. C. F. Müller-Wodarg et al. 2019). The strong field on Jupiter allows for sufficiently strong ion–neutral drag to slow down the zonal neutral winds in the thermosphere and break the zonal flow-dominated pattern that we see on Saturn and that "traps" energy near the poles on Saturn. Thereby, the planetary ***B***-field on Jupiter facilitates global energy redistribution by meridional winds and explains the large observed temperatures at low and midlatitudes on Jupiter. Our calculations show that the temperatures can easily be accounted for by the energy deriving from magnetosphere–ionosphere coupling. Thereby, no "energy crisis" appears to exist on Jupiter. This will still allow for other energy sources at low and midlatitudes on Jupiter, such as gravity waves and acoustic waves (L. A. Young et al. 1997; K. I. Matcheva & D. F. Strobel 1999; G. Schubert et al. 2003), but does not require these other energy sources in order to explain the thermal structure at low and midlatitudes. Through our study, we have highlighted how the strength of a planetary internal ***B***-field may fundamentally impact the horizontal thermal structure of its upper atmosphere. Beyond our solar system, this may also impact our understanding of exoplanet atmospheres and perhaps help constrain the magnitude of their ***B***-field from their atmosphere's thermal structure.

Acknowledgments

The authors wish to thank the reviewer for the very helpful comments that have contributed greatly to the quality of the manuscript. I.M.W. and P.I. acknowledge funding from the UK Science and Technology Facilities Council grant no. ST/W001071/1.

Appendix
The JTIM Model

GCMs simulate the global coupling of all processes in an atmospheric system by solving the coupled nonlinear Navier–Stokes equations of momentum, energy, and continuity. GCMs are physical models that make few assumptions beyond those intrinsic to their fundamental equations (e.g., fluid and hydrostatic behavior), boundary conditions, basic gas parameters (reaction rates, heating efficiencies), and external inputs such as solar EUV flux and other heating and any momentum sources and sinks not captured by the intrinsic processes included in the code. They calculate in a physically self-consistent manner the time-dependent response of atmospheric gases to such external inputs. For reasons of computational efficiency, some processes need to be parameterized. Any approximations are clarified in the following.

A.1. Momentum Equation

JTIM numerically solves the coupled 3D Navier–Stokes equations of momentum, energy, and continuity above 9.5 Pa (200 km) by explicit time integration. The two horizontal components of the momentum equation in spherical pressure coordinates are the same as in the STIM model (I. C. F. Müller-Wodarg et al. 2012, 2019) and given by

$$\begin{aligned}\frac{\partial u_\theta}{\partial t} = &-\left(u_\theta \frac{1}{a}\frac{\partial u_\theta}{\partial \theta} + u_\phi \frac{1}{a \cdot \sin\theta}\frac{\partial u_\theta}{\partial \phi} + w\frac{\partial u_\theta}{\partial p}\right) \\ &+ \left(\frac{w u_\theta}{a\rho g} + \frac{u_\phi^2}{a \cdot \tan\theta}\right) - \frac{g}{a}\frac{\partial h_p}{\partial \theta} \\ &+ 2\Omega u_\phi \cos\theta + \frac{1}{\rho}\mu \nabla_p^2 \quad u_\theta \\ &+ \frac{g}{a^2}\frac{\partial}{\partial p}\left(a^2 \mu\rho g \frac{\partial u_\theta}{\partial p}\right) + \frac{B_r}{\rho} j_\phi,\end{aligned} \tag{A1}$$

$$\begin{aligned}\frac{\partial u_\phi}{\partial t} = &-\left(u_\theta \frac{1}{a}\frac{\partial u_\phi}{\partial \theta} + u_\phi \frac{1}{a \cdot \sin\theta}\frac{\partial u_\phi}{\partial \phi} + w\frac{\partial u_\phi}{\partial p}\right) \\ &- \left(\frac{-w u_\phi}{a\rho g} + \frac{u_\theta u_\phi}{a \cdot \tan\theta}\right) - \frac{g}{a \cdot \sin\theta}\frac{\partial h_p}{\partial \phi} \\ &- 2\Omega u_\theta \cos\theta + \frac{1}{\rho}\mu \nabla_p^2 \quad u_\phi \\ &+ \frac{g}{a^2}\frac{\partial}{\partial p}\left(a^2 \mu\rho g \frac{\partial u_\phi}{\partial p}\right) - \frac{B_r}{\rho} j_\theta.\end{aligned} \tag{A2}$$

Here, u_θ and u_ϕ are the neutral wind components, defined as positive southward and eastward, respectively; a is the distance to the center of the planet; θ is the colatitude; ϕ is the longitude; h_p is the height of the pressure level; and t is time. Furthermore, g is the (height-dependent) gravitational acceleration, ρ is the mass density, p is the pressure, Ω is Jupiter's rotation period (with $\Omega = 1.7585 \cdot 10^{-4}\,\mathrm{s}^{-1}$, corresponding to 9.925 hr), and μ is the coefficient of viscosity. We calculate viscosities using the same technique and coefficients as N. Achilleos et al. (1998). w is the vertical wind in the pressure frame, defined as $w = dp/dt$. The total vertical velocity in the height frame, u_z, is obtained by adding the velocity of the pressure level itself (barometric velocity) to the velocity relative to the pressure level (divergence velocity), $-1/(\rho g)w$: $u_z = (\partial h_p/\partial t) - 1/(\rho g)w$.

$\boldsymbol{\nabla}_p$ is the 2D gradient operator on a level of fixed pressure. For its square, we use the expression

$$\nabla_p^2 = \frac{1}{a^2}\frac{\partial^2}{\partial\theta^2} + \frac{\cos\theta}{a^2\sin\theta}\frac{\partial}{\partial\theta} + \frac{1}{a^2\sin^2\theta}\frac{\partial^2}{\partial\phi^2}. \tag{A3}$$

In the vertical direction, the pressure gradient and gravity acceleration dominate other terms by several orders of magnitude, and an accurate numerical calculation of the vertical velocity w by solving the vertical component of the momentum equation is numerically difficult. Vertical winds are therefore calculated using the continuity equation, which in the pressure coordinate system reduces to the simple form of

$$\frac{1}{a\cdot\sin\theta}\frac{\partial}{\partial\theta}u_\theta\sin\theta + \frac{1}{a\cdot\sin\theta}\frac{\partial u_\phi}{\partial\phi} + \frac{\partial w}{\partial p} = 0. \tag{A4}$$

Physically, the equation expresses that any divergence or convergence in the horizontal velocity field must be balanced by vertical wind in order to conserve mass. To calculate w, we use the technique described by I. C. F. Müller-Wodarg et al. (2000), integrating from the top boundary of the model (where we set $w = 0$) down. As boundary conditions for the horizontal momentum equation, we assume fixed wind velocities (of zero) at the bottom and vanishing vertical gradients of wind components at the top level.

The last terms on the right side of Equations (A1) and (A2) represent ion drag, or exchange of momentum between the neutral gases and surrounding ions. In the absence of electric or magnetic fields, the collisions between ions and neutral gases would lead to the ions moving alongside the neutrals. When a B-field is present and the gyrofrequencies of the ions are comparable to or larger than the ion–neutral collision frequencies, the motion of ions is constrained by the B-fields, potentially causing the neutral winds to be slowed down. When an external electric field is present, it can accelerate the ions and electrons, potentially causing an acceleration of the neutral gases as well. It is therefore important to include this momentum term in JTIM, as it forms the core for properly accounting for magnetosphere–atmosphere coupling.

The ion drag term can, in general, be expressed as

$$\boldsymbol{a}_{ni} = -\nu_{ni}(\boldsymbol{u} - \boldsymbol{v}), \tag{A5}$$

where $\boldsymbol{a}_{ni}$ denotes the acceleration due to neutral–ion collisions in the atmosphere, ν_{ni} is the neutral–ion collision frequency, and $\boldsymbol{u}$ and $\boldsymbol{v}$ are the neutral and ion velocities, respectively. In our model, we implement the ion drag term in a different form, following the procedure used by T. J. Fuller-Rowell & D. Rees (1980, 1981), whereby the ion drag term is instead expressed as a function of the current density $\boldsymbol{J}$ in the ionosphere,

$$\boldsymbol{a}_{ni} = -\nu_{ni}(\boldsymbol{u} - \boldsymbol{v}) = \frac{1}{\rho}\boldsymbol{J}\times\boldsymbol{B}, \tag{A6}$$

where $\boldsymbol{B}$ denotes Jupiter's internal magnetic field and ρ is the atmospheric neutral mass density. We use the JRM33 B-field model of J. E. P. Connerney et al. (2022) in JTIM and the resulting magnetic coordinate system derived by Y. Wang et al. (2023).

We calculate the current density $\boldsymbol{J}$ by using a generalization of Ohm's law,

$$\boldsymbol{J} = \underline{\sigma}\cdot(\boldsymbol{E} + \boldsymbol{u}\times\boldsymbol{B}), \tag{A7}$$

where $\underline{\sigma}$ denotes the 3×3 conductivity tensor, $\boldsymbol{E}$ is an externally applied electric field (or internal polarization field, not currently included in JTIM), and $\boldsymbol{u}\times\boldsymbol{B}$ represents the dynamo field. Thus, $(\boldsymbol{E} + \boldsymbol{u}\times\boldsymbol{B})$ is the electric field in the neutral rest frame. Following H. Rishbeth & O. K. Garriott (1969), we assume the concept of layer conductivities, whereby the conducting layer is assumed to have a limited vertical extent and may thus instead be expressed as a 2×2 tensor in the horizontal (latitudinal, zonal), given by

$$\underline{\sigma} = \begin{bmatrix} \sigma_\mathrm{P}/\sin^2(I) & \sigma_\mathrm{H}/\sin(I) \\ -\sigma_\mathrm{H}/\sin(I) & \sigma_\mathrm{P} \end{bmatrix}. \tag{A8}$$

Here, σ_P and σ_H denote the Pedersen and Hall conductivities, respectively, and I is the dip angle of the magnetic field $\boldsymbol{B}$. We calculate σ_P and σ_H self-consistently in the model at every grid point using the basic expressions as given by H. Rishbeth & O. K. Garriott (1969). Combining the 2D version of Equation (A7) with Equation (A8) yields expressions for the latitudinal (j_θ) and longitudinal (j_ϕ) components of the current density as

$$j_\theta = \frac{\sigma_P}{\sin^2(I)}(E_\theta + u_\phi B_r) - \frac{\sigma_H}{\sin(I)}(-E_\phi + u_\theta B_r) \tag{A9}$$

and

$$j_\phi = \sigma_P(E_\phi - u_\theta B_r) - \frac{\sigma_H}{\sin(I)}(E_\theta + u_\phi B_r), \tag{A10}$$

where E_θ and E_ϕ denote meridional and zonal components of the electric convection or polarization field and B_r is the radial magnetic field. In JTIM, we calculate the current densities every few time steps and use Equations (A9) and (A10) in the ion drag terms of the momentum Equations (A1) and (A2).

A.2. Energy Equation

The energy balance is given by the sum of the internal and external energy sources and sinks. In a spherical pressure coordinate system, it may be expressed by the relation

$$\begin{aligned}
&\frac{\partial\epsilon}{\partial t} + \boldsymbol{U}_p\cdot\nabla_p(\epsilon + gh_p) + w\,\frac{\partial(\epsilon + gh_p)}{\partial p} \\
&= Q_\mathrm{EUV} + Q_\mathrm{IR} + Q_\mathrm{Joule} \\
&+ \frac{g}{a^2}\frac{\partial}{\partial p}\left(a^2\frac{(K_m + K_\tau)}{H}\,p\,\frac{\partial T}{\partial p}\right) \\
&+ \frac{1}{\rho}(K_m + K_\tau)\,\nabla_p^2 T \\
&+ u_\theta\frac{g}{a^2}\frac{\partial}{\partial p}\left(a^2\mu\rho g\frac{\partial u_\theta}{\partial p}\right) \\
&+ u_\phi\frac{g}{a^2}\frac{\partial}{\partial p}\left(a^2\mu\rho g\frac{\partial u_\phi}{\partial p}\right).
\end{aligned} \tag{A11}$$

Here ϵ is the sum of the internal and kinetic energies per unit mass, defined as $\epsilon = c_p\,T + 0.5\,(u_\theta^2 + u_\phi^2)$, and T is the gas temperature. With gh_p representing the potential energy of the gas at height h_p, the term $\epsilon + gh_p$ is thus its enthalpy. Coefficients of molecular conduction (K_m) are equivalent to those of N. Achilleos et al. (1998) and turbulent conduction set to $K_\tau = c_p\,\rho\,K$.

Q_EUV is heating due to solar EUV and far-UV radiation that is absorbed by H_2, H, and He at wavelengths between 7.5 and around 103.2 nm, in particular the He II line (30.38 nm). We derive solar EUV heating rates by explicit calculation of photon absorption along ray paths through the atmosphere, assuming a heating efficiency of 50% for all constituents and wavelengths (J. H. Waite et al. 1983). Another implicit assumption in these heating rate calculations is that thermal energy is released where the photons are absorbed. Neither this nor the assumed heating efficiencies pose any significant limitations for our current purpose, given the overall low importance of direct solar heating in Jupiter's thermosphere. We use absorption cross sections consistent with those of J. I. Moses et al. (2000) and solar EUV fluxes from the SOLAR2000 model (W. K. Tobiska 2004).

Radiative cooling Q_{IR} in Jupiter's thermosphere occurs via thermal emissions from H_3^+, one of the important ions in giant planet atmospheres like Jupiter (H. Melin et al. 2006; S. Miller et al. 2010). We adopt the parameterization of H_3^+ cooling by S. Miller et al. (2013) in JTIM. Radiative transfer calculations are not needed in the thermosphere of Jupiter. As boundary conditions for the energy equation, we assume a fixed temperature (165 K) at the bottom and zero vertical temperature gradients at the top.

Q_{Joule} is the Joule heating term and, alongside the momentum equation's ion drag terms, constitutes a link between the magnetosphere and atmosphere. When currents flow in the ionosphere, an environment that is not perfectly conducting, resistive heating occurs, a process often referred to as Joule heating. Following the treatment of T. J. Fuller-Rowell & D. Rees (1981), we express the rate of Joule heating per unit mass using the relation

$$Q_{\mathrm{Joule}} = \frac{1}{\rho}(\boldsymbol{J}\cdot\boldsymbol{E}) = \frac{1}{\rho}(j_\theta E_\theta + j_\phi E_\phi). \tag{A12}$$

Note that the electrical current $\boldsymbol{J}$ in the Joule heating term (Equation (A7)) includes the effect of neutral winds. Physically, this means that the above expression for Joule heating consists of two components, the thermal heating of the atmosphere by electrical currents and the change of kinetic energy of the atmospheric gases that results from the momentum change from ion drag (Equation (A6)). While the thermal heating by currents alone can only be a positive quantity, the Q_{Joule} that includes the effect of winds can also attain negative values, implying loss of kinetic energy of the neutral atmosphere (V. M. Vasyliunas & P. Song 2005).

The external electric field $\boldsymbol{E}$ originates from the departure of regions in Jupiter's magnetosphere from corotation due to plasma production from internal sources. Thus, $\boldsymbol{E}$ represents a key parameter determining the coupling between magnetosphere and ionosphere. In a fully two-way coupled ionosphere–magnetosphere model, the value of $\boldsymbol{E}$ would change in response to atmospheric conditions, but we currently do not include this feedback in our model and define a time-independent profile of $\boldsymbol{E}$.

We apply an external electric field based on S. W. H. Cowley et al. (2005) as shown in Figure 5 that can be scaled in overall strength via a user-applied factor. The field shown in Figure 5 applies a factor of 0.55, which was determined on the basis of resulting auroral temperature values. In our standard simulation shown in this study, the maximum electric field strength is around 1.2 V m^{-1}. The figure shows the E_θ component, and we assume $E_\phi = 0$ in the magnetic frame, in line with the assumptions by S. W. H. Cowley et al. (2005) of axisymmetry around the magnetic axis. E_θ is constant in time in the magnetic reference frame, but in reality, it may change with time and add variability to the upper atmosphere. Also, we do not currently consider any moon footprints. JTIM allows for the future implementation of a more realistic 2D electric potential field pattern from Jupiter MHD models such as BATSrUS (Y. Sarkango et al. 2019) that will include components in both E_θ and E_ϕ.

A.3. Neutral and Ion Composition

In addition, our model allows for the dynamical redistribution of individual gases by explicitly calculating their transport by winds and molecular and eddy diffusion. While transport by winds is treated both horizontally and vertically, we calculate molecular and eddy diffusion only in the vertical direction, since vertical gradients are much larger than horizontal gradients, making horizontal diffusion negligible. The molecular diffusion velocities are given by

$$\frac{\partial Y_i}{\partial z} - \left(1 - \frac{m_i}{m} - \frac{H}{m}\frac{\partial m}{\partial z}\right)\frac{Y_i}{H} = -\sum_{j\neq i}\frac{mY_iY_j}{m_jD_{ij}}(w_i^D - w_j^D), \tag{A13}$$

where $Y_i = \rho_i/\rho$ and m_i are the mass fraction and molecular mass of the ith constituent, m is the mean molecular mass of the atmosphere, H is the pressure scale height, D_{ij} is the binary diffusion coefficient, and w_i^D is the vertical diffusion velocity of the ith constituent (S. Chapman & T. G. Cowling 1970). Molecular constituents are also subject to eddy diffusion, which we calculate with

$$w_i^K = -K\frac{\partial \ln(Y_i)}{\partial z}, \tag{A14}$$

where K is the eddy diffusion coefficient. Here, K represents mixing due to small-scale motions not resolved by the model. The diffusion velocities are then used in the continuity equation to calculate the time development of mass fractions. The continuity equation for the ith constituent is given in spherical pressure coordinates by

$$\frac{\partial Y_i}{\partial t} + u_\theta\frac{1}{a}\frac{\partial Y_i}{\partial \theta} + u_\phi\frac{1}{a\cdot\sin\theta}\frac{\partial Y_i}{\partial \phi} + w\frac{\partial Y_i}{\partial p} = \frac{g}{a^2}\frac{\partial}{\partial p}(a^2\rho Y_i(w_i^D + w_i^K)) + J_i, \tag{A15}$$

where J_i is the net chemical source rate (R. E. Dickinson & E. C. Ridley 1975). The velocities u_θ, u_ϕ, and w represent the mean velocity of the atmosphere, defined as the average of the velocities of individual constituents, weighted by their mass densities.

Our GCM gas transport calculations include the species H_2, H, and He, and we assume fixed height-dependent mixing ratios for CH_4 and for H_2O from J. I. Moses et al. (2005). JTIM includes a scheme of ion–neutral chemistry (L. E. Moore et al. 2004) and calculates the densities of ions H^+, H_2^+, H_3^+, He^+, CH_3^+, CH_4^+, CH_5^+, H_2O^+, and H_3O^+, assuming the ionization cross sections and chemical reaction rates described by L. E. Moore et al. (2004). The charge-exchange reaction of H^+ with vibrationally excited H_2 ($\nu \geqslant 4$) is adopted from

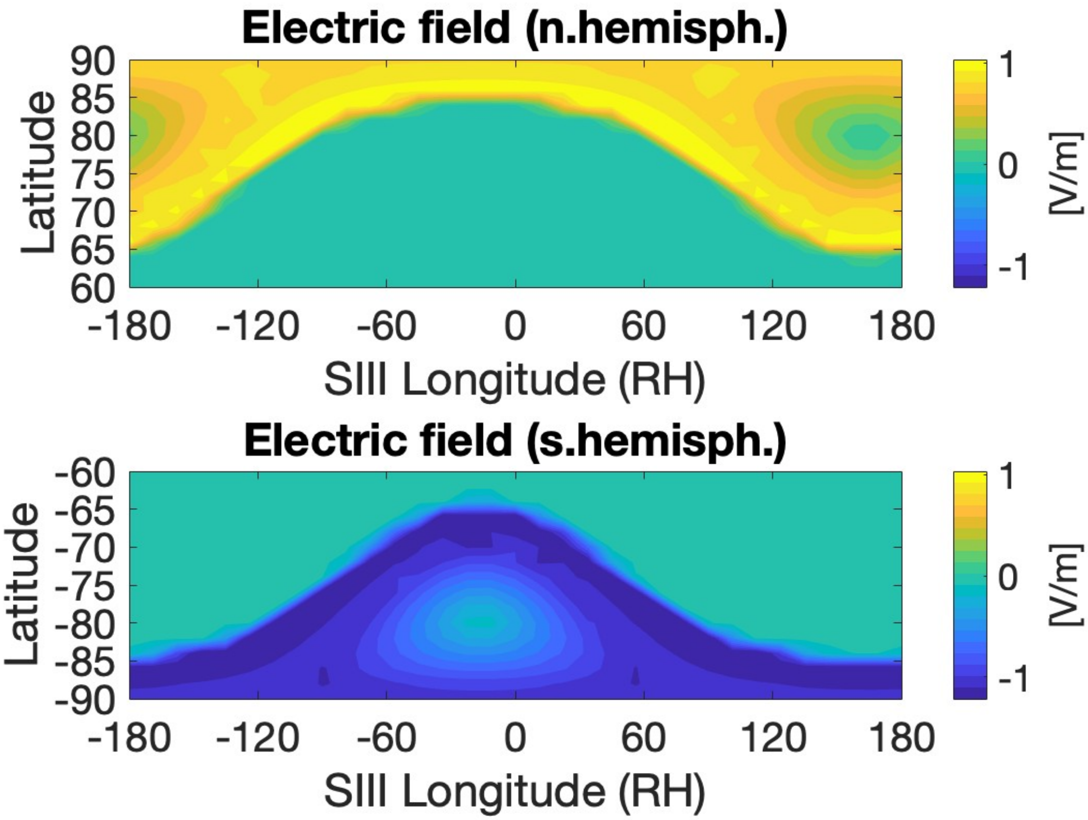

Figure 5. North–south electric field strength applied in the auroral regions of JTIM. Values are positive southward. The latitudinal structure is based on that of S. W. H. Cowley et al. (2005) and follows the magnetic field geometry. The x-axis is in System III (SIII) longitude (right-handed).

Equation (7) of L. E. Moore et al. (2004) and scaled up by a factor of $2^2 = 4$ to account for the factor of 2 closer proximity of Jupiter to the Sun.

At auroral latitudes (10°–16° magnetic colatitude; see also Figure 6), we include particle ionization from suprathermal electrons. We currently use the parameterization of D. Grodent et al. (2001), which assumes an electron population at three energies, $E_1 = 15$ keV ($\Phi_1 = 0.02$ J m^{-2} s^{-1}), $E_2 = 3$ keV ($\Phi_2 = 0.01$ J m^{-2} s^{-1}), and $E_3 = 100$ eV ($\Phi_3 = 5 \times 10^{-4}$ J m^{-2} s^{-1}). The overall flux can be scaled by the user. Height-integrated production rates of H_2^+ are shown in Figure 6, illustrating the relative importance of solar and particle impact ionization at different latitudes.

The ionosphere in JTIM varies globally and with time, responding self-consistently to variations in solar flux, energetic electron precipitation flux, and neutral composition. The resulting Pedersen conductances are shown in Figure 7 and play a key role in magnetosphere–ionosphere–thermosphere coupling.

Molecular diffusion coefficients are calculated using the standard expression $D_{ij} = A_{ij} T^{s_{ij}} / n_j$ [cm^2 s^{-1}], where n_j is the major gas density and A_{ij} for pairs H_2–H, H_2–He, and He–H are, in cgs units, given by $8.19 \cdot 10^{17}$, $6.45 \cdot 10^{17}$, and $8.84 \cdot 10^{17}$ (P. M. Banks & G. Kockarts 1973; P. A. Bernhardt 1979). For the same gas pairs, values for s_{ij} are 0.728, 0.716, and 0.706, respectively. We ignore self-diffusion ($A_{ii} = A_{jj} = 0$) and assume $A_{ij} = A_{ji}$.

Values for the eddy diffusion coefficient have been discussed in detail by J. I. Moses et al. (2005) and were found to range from 1 to 100 m^2 s^{-1} in the region above the JTIM lower boundary and the homopause. We have adopted a height-independent eddy diffusion coefficient of $K = 100\,\mathrm{m^2\,s^{-1}}$ in JTIM. This places the homopause near the 10 μbar level, or around 310 km altitude.

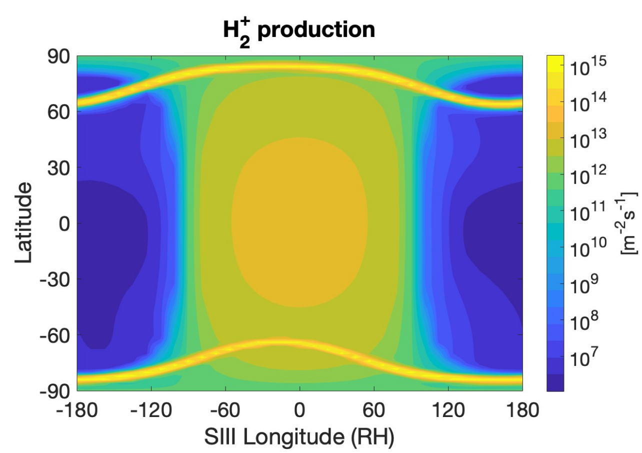

Figure 6. Height-integrated H_2^+ production rates in JTIM. The energetic electron precipitation production rates at auroral latitudes are taken from D. Grodent et al. (2001) and applied at 15° magnetic colatitude with a Gaussian distribution assuming $\sigma = 0.^\circ 6$ latitude. Height-integrated electron impact ionization rates exceed the dayside solar ionization rates by around 2 orders of magnitude. The figure shows a snapshot at 12 UT, and over the course of a Jupiter day, the solar-controlled region will move relative to the magnetic-field-controlled auroral precipitation geometry. The x-axis is in System III (SIII) longitude (right-handed).

Our global spherical grid allows for flexible horizontal and vertical resolution, and the present calculations assume spatial resolutions of 2° latitude by $11.^\circ 25$ longitude by 0.4 scale

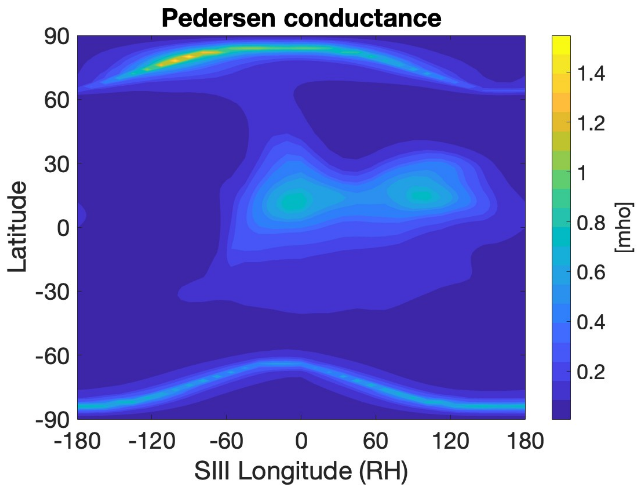

Figure 7. Pedersen conductances in Jupiter's ionosphere, as simulated by JTIM. The larger conductances in the northern auroral region are a result of the magnetic field asymmetries, whereby reduced magnetic field strength leads to enhanced conductances. We assume the JRM33 magnetic field of J. E. P. Connerney et al. (2022). Magnetic field variations also cause the two distinct local maxima in conductance at equatorial latitudes. The snapshot is for UT = 12, whereby System III (SIII) longitude = 0 is at local noon and dusk is at SIII longitude = 90°.

heights vertically with 48 vertical levels in total and integrate with a 1 s time step. Each simulation is run to near steady state for 85 Jupiter rotations.

ORCID iDs

Ingo C. F. Müller-Wodarg https://orcid.org/0000-0001-6308-7826
Peio Iñurrigarro https://orcid.org/0000-0001-7773-2275
Luke Moore https://orcid.org/0000-0003-4481-9862
Tommi T. Koskinen https://orcid.org/0000-0003-3071-8358
Alexander S. Medvedev https://orcid.org/0000-0003-2713-8977

References

Achilleos, N., Miller, S., Tennyson, J., et al. 1998, JGR, 103, 20089
Bagenal, F. 2013, in Planetary Magnetospheres, ed. T. D. Oswalt, L. M. French, & P. Kalas (Dordrecht: Springer), 251
Banks, P. M., & Kockarts, G. 1973, Aeronomy (New York: Academic Press)
Bernhardt, P. A. 1979, JGR, 84, 793
Bonfond, B., Yao, Z., & Grodent, D. 2020, JGRA, 125, e28152
Bougher, S. W., Waite, J. H., Majeed, T., & Gladstone, G. R. 2005, JGRE, 110, E04008
Broadfoot, A. L., Belton, M. J. S., Takacs, P. Z., et al. 1979, Sci, 204, 979
Brown, Z. L., Medvedev, A. S., Starichenko, E. D., Koskinen, T. T., & Müller-Wodarg, I. C. F. 2022, GeoRL, 49, e2021GL097219
Chapman, S., & Cowling, T. G. 1970, The Mathematical Theory of Non-uniform Gases. An Account of the Kinetic Theory of Viscosity, Thermal Conduction and Diffusion in Gases (Cambridge, UK: Cambridge Univ. Press)
Connerney, J. E. P., Timmins, S., Oliversen, R. J., et al. 2022, JGRE, 127, e07055
Cowley, S. W. H., Alexeev, I. I., Belenkaya, E. S., et al. 2005, JGRA, 110, A11209
Cowley, S. W. H., & Bunce, E. J. 2001, P&SS, 49, 1067
Davis, L. J., & Smith, E. J. 1990, JGR, 95, 15257
Dickinson, R. E., & Ridley, E. C. 1975, JAtS, 32, 1219
Drossart, P., Maillard, J. P., Caldwell, J., et al. 1989, Natur, 340, 539
Fuller-Rowell, T. J., & Rees, D. 1980, JAtS, 37, 2545
Fuller-Rowell, T. J., & Rees, D. 1981, JATP, 43, 701
Grodent, D., Waite, J. H., Jr., & Gérard, J.-C. 2001, JGR, 106, 12933
Hill, T. W. 1980, Sci, 207, 301
Iñurrigarro, P., Medvedev, A. S., Müller-Wodarg, I. C. F., & Moore, L. 2024, GeoRL, 51, e2024GL110883
Majeed, T., Waite, J. H., Bougher, S. W., & Gladstone, G. R. 2009, JGRE, 114, E07005
Matcheva, K. I., & Strobel, D. F. 1999, Icar, 140, 328
Melin, H., Miller, S., Stallard, T., Smith, C., & Grodent, D. 2006, Icar, 181, 256
Miller, S., Stallard, T., Melin, H., & Tennyson, J. 2010, FaDi, 147, 283
Miller, S., Stallard, T., Tennyson, J., & Melin, H. 2013, JPCA, 117, 9770
Moore, L. E., Mendillo, M., Müller-Wodarg, I. C. F., & Murr, D. L. 2004, Icar, 172, 503
Moses, J. I., Bézard, B., Lellouch, E., et al. 2000, Icar, 143, 244
Moses, J. I., Fouchet, T., Bézard, B., et al. 2005, JGRE, 110, E08001
Müller-Wodarg, I. C. F., Koskinen, T. T., Moore, L., et al. 2019, GeoRL, 46, 2372
Müller-Wodarg, I. C. F., Mendillo, M., Yelle, R. V., & Aylward, A. D. 2006, Icar, 180, 147
Müller-Wodarg, I. C. F., Moore, L., Galand, M., Miller, S., & Mendillo, M. 2012, Icar, 221, 481
Müller-Wodarg, I. C. F., Yelle, R. V., Mendillo, M., Young, L. A., & Aylward, A. D. 2000, JGR, 105, 20833
O'Donoghue, J., Moore, L., Bhakyapaibul, T., et al. 2021, Natur, 596, 54
Prangé, R. 1992, AdSpR, 12, 379
Rishbeth, H., & Garriott, O. K. 1969, Introduction to Ionospheric Physics (Cambridge, UK: Cambridge Univ. Press)
Sarkango, Y., Jia, X., & Toth, G. 2019, JGRA, 124, 5317
Schubert, G., Hickey, M. P., & Walterscheid, R. L. 2003, Icar, 163, 398
Seiff, A., Kirk, D. B., Knight, T. C. D., et al. 1997, Sci, 276, 102
Smith, C. G. A., Aylward, A. D., Millward, G. H., Miller, S., & Moore, L. E. 2007, Natur, 445, 399
Stallard, T., Miller, S., Millward, G., & Joseph, R. D. 2001, Icar, 154, 475
Strobel, D. F. 2002, in Aeronomic Systems on Planets, Moons, and Comets, ed. M. Mendillo, A. Nagy, & J. H. Waite (New York: Wiley), 7
Tao, C., Fujiwara, H., & Kasaba, Y. 2009, JGRA, 114, A08307
Tobiska, W. K. 2004, AdSpR, 34, 1736
Vasyliunas, V. M., & Song, P. 2005, JGRA, 110, A02301
Vriesema, J. W., Koskinen, T. T., & Yelle, R. V. 2020, Icar, 344, 113390
Waite, J. H., Cravens, T. E., Kozyra, J., et al. 1983, JGR, 88, 6143
Wang, Y., Wang, Y., Tang, K., & Kong, D. 2023, E&SS, 10, e2023EA003147
Yates, J. N., Ray, L. C., Achilleos, N., Witasse, O., & Altobelli, N. 2020, JGRA, 125, e26792
Yelle, R. V., & Miller, S. 2004, in Jupiter. The Planet, Satellites and Magnetosphere, ed. F. Bagenal, T. E. Dowling, & W. B. McKinnon, Vol. 1 (Cambridge: Cambridge Univ. Press), 185
Young, L. A., Yelle, R. V., Young, R., Seiff, A., & Kirk, D. B. 1997, Sci, 276, 108